



## Multiscale analysis of an ODS FeAl40 intermetallic after plasma-assisted nitriding

J. Martin, A. Martinavicius, S. Bruyère, H.P. van Landeghem, C. Gendarme, F. Danoix, Raphaële Danoix, A. Redjaïmia, T. Grosdidier, T. Czerwicz

### ► To cite this version:

J. Martin, A. Martinavicius, S. Bruyère, H.P. van Landeghem, C. Gendarme, et al.. Multiscale analysis of an ODS FeAl40 intermetallic after plasma-assisted nitriding. *Journal of Alloys and Compounds*, 2016, 683, pp.418-426. <10.1016/j.jallcom.2016.05.119>. <hal-01614346>

**HAL Id: hal-01614346**

**<https://hal.science/hal-01614346v1>**

Submitted on 25 Jan 2023

**HAL** is a multi-disciplinary open access archive for the deposit and dissemination of scientific research documents, whether they are published or not. The documents may come from teaching and research institutions in France or abroad, or from public or private research centers.

L'archive ouverte pluridisciplinaire **HAL**, est destinée au dépôt et à la diffusion de documents scientifiques de niveau recherche, publiés ou non, émanant des établissements d'enseignement et de recherche français ou étrangers, des laboratoires publics ou privés.



HAL Authorization

## **Multiscale analysis of an ODS FeAl40 intermetallic after plasma-assisted nitriding**

J. Martin<sup>1,\*</sup>, A. Martinavicius<sup>1,2</sup>, S. Bruyère<sup>1</sup>, H. P. Van Landeghem<sup>1</sup>, C. Gendarme<sup>1</sup>,  
F. Danoix<sup>2</sup>, R. Danoix<sup>2</sup>, A. Redjaimia<sup>1</sup>, T. Grosdidier<sup>1</sup>, T. Czerwicz<sup>1</sup>

<sup>1</sup> Université de Lorraine, Laboratoire d'Excellence Design of Alloy Metals for low-mAss Structures ('LabEx DAMAS'), Institut Jean Lamour (UMR CNRS 7198), Laboratoire LEM3 (UMR CNRS 7239), Ile de Saulcy, F-57045 Metz

<sup>2</sup> Université de Rouen, UMR CNRS 6634, Avenue de l'Université, F-76801 Saint Etienne du Rouvray

\*Corresponding author: +33 383 584 251, [julien.martin@univ-lorraine.fr](mailto:julien.martin@univ-lorraine.fr)

## Abstract

The binary B2 (ordered bcc-type structure) FeAl40 Grade 3 aluminide containing 40 at.% Al was nitrided at 600 °C for 15 min with a pulsed DC plasma in a 95% N<sub>2</sub> / 5% H<sub>2</sub> gas mixture. The nitrided layer was described at the micro-, nano- and atomic scales. The nitrided layer consists of a thin outer sublayer (~1 µm in thickness) containing  $\gamma'$ -Fe<sub>4</sub>N and having a moderate hardness (870 Hv) below which a thicker (~36 µm in thickness) and harder (1400 Hv) inner sublayer is formed. While the outer sublayer is completely depleted in Al, the inner sublayer is made of a mixture of hex. AlN and  $\alpha$ -Fe phases regularly structured at different levels: i) At the micrometre scale, observations showed a network of  $\alpha$ -Fe “wave-like” veins (~2 µm in length and ~100 nm in width) located at the grain boundaries and preferentially aligned parallel to the nitrided surface. ii) At the nanometre scale, observations evidenced that such veins are embedded in a “lamellar-like” morphology matrix alternately composed of  $\alpha$ -Fe and  $\alpha$ -Fe/hex. AlN lamellae (~300 nm in length and ~10 nm in width). iii) At the atomic scale, analysis pointed out that each  $\alpha$ -Fe / hex. AlN lamella presents a finer structural arrangement in which hex. AlN-rich clusters (~4 nm in diameter) are trapped between thin  $\alpha$ -Fe walls (~2 nm in thickness). The diversity of the morphologies evidenced in the present study highlights the complexity of the nitriding mechanisms of iron-based aluminides. The observations support however a mechanism of discontinuous precipitation in the inner nitrided sublayer which seems to be strongly promoted by the high amount of Al in the FeAl40 grade 3 alloy (40 at.%).

**Keywords:** Intermetallic; Fe-Al alloy; Plasma nitriding; discontinuous precipitation; Transmission electron microscopy; Atom probe tomography

## 1. Introduction

Binary B2 iron aluminides (Fe-Al) are attractive intermetallic compounds as lightweight and structural materials [1]. However, they are rather brittle at room temperature and offer poor strength and creep resistance at high temperature. Efforts have been devoted to improve these properties for applications in the ambient to 600 °C temperature range [2]. A significant progress has consisted in developing an oxide dispersed strengthened (ODS) creep resistant version of the FeAl intermetallic, the FeAl Grade 3 alloy, from a powder metallurgy route involving ball milling followed by hot extrusion at 1100 °C [3]. From micro-alloying with Zr and B combined with the fine dispersion of the nanometre size  $Y_2O_3$  resulting in a grain size reduction, the grain boundary strength was also optimised [3,4] while the oxidation resistance was improved [5,6]. Other processing powder metallurgy routes including consolidation by forging, rolling or swaging [7], spark plasma sintering [8, 9], thermal spraying [10, 11] and even additive manufacturing [12] have been attempted. The development of this new generation of Al-rich B2 FeAl alloys has raised some hopes for promising applications as a substitution material of steels and superalloys for the fabrication of transmission shafts, brakes or valves for the aerospace and automotive industries as well as protective coatings for heat exchangers or piping [3, 13].

Although major progresses have been made in improving the mechanical properties of these B2 iron aluminides and despite some additional attempts to play with the microstructure for improving ductility [14] and/or texture for improving stiffness [15-17], these alloys often still suffer from a major lack of ductility due to (i) a well-known moisture induced environmental embrittlement [18, 19], a high temperature brittle-to-ductile transition temperature (BDTT) at high (41-45 at%) Al contents [20]

or a lack of cohesion at the former inter-particle boundaries in powder processed materials [21]. In addition, the wear resistance of iron aluminides remain poor due to the insufficient surface hardness [22, 23]. This additional handicap could slow down their future applications in which high loads and strong surface contacts are applied to the FeAl structural material. Thus, several studies have proposed surface engineering approaches such as thermal oxidation [19, 24, 25], boronizing [26] and nitriding treatments (gaseous atmosphere, ion implantation, plasma-assisted) [27-29] to improve the surface hardness. At the same time, as was proved by mechanical tests on pre-oxidized samples of B2 iron aluminides [19, 25], these techniques should provide a physical protecting layer to avoid the moisture-induced embrittlement originating from the interaction, at the crack tip, of the aluminium atoms with the hydrogen contained in the environment.

Among all the previously mentioned surface treatment processes, it has been shown that the nitriding treatments are the most promising for hardening and that they lead to thick and compact protective layers. In order to better understand the response of the B2 FeAl alloy to nitriding, particularly those containing large amounts of Al, few pioneer studies have been conducted to gain a deeper scientific understanding of the mechanisms involved during the growth of the nitride layers [27-29]. Owing to the complexity of the nitride microstructures in the B2 alloys, it is likely that the possible proposed mechanisms for nitriding remain still debateable mainly due to the fact that the nitrified FeAl microstructure has not yet been observed and described at very local scales. To this end, the present paper reports a detailed multi-scale description of the ODS FeAl (40 at. % Al), the FeAl40 grade 3 model alloy, nitrified at 600 °C for 15 min within a pulsed d.c. plasma nitrogen discharge. Complementary analytical techniques,

such as scanning electron microscopy (SEM), electron probe micro-analysis (EPMA), grazing-incidence X-ray diffraction (GIXRD), transmission electron microscopy (TEM) and atomic probe tomography (APT), were used to depict the chemical and morphological description of the nitrided layer at various scales, from the micrometre to the atomic scale. In addition, micro-hardness measurements were carried out to ensure that nitriding was successfully applied and to confirm the duplex nature of the nitride layer that was, in fact, depicted as two successive layers through the nitride depth.

## **2. Material and methods**

The investigated material is an ODS aluminide intermetallic alloy manufactured using powder metallurgy route under the reference FeAl40 Grade 3 (Fe-40 at.% Al) [3]. Plasma nitriding was performed at 600 °C for 15 min using a 800 Hz pulsed d.c. discharge with a 0.8 duty cycle ratio [30]. The plasma was ignited in a 95% N<sub>2</sub> – 5% H<sub>2</sub> gas mixture under a 180 Pa pressure.

Mechanical properties of the nitrided layer were evaluated with hardness measurements using a Duramin micro-indenter (Struers). In-depth micro-hardness profiles were performed on cross-section using a constant load (100 g). Complementary to these cross-section measurements, the topmost surface hardness of the nitrided layer was also investigated by indenting the surface with increasing loads (50, 100, 300, 500 and 1000 g) and the recorded hardness were related to an equivalent penetration depth [31, 32]. In this way, from top surface hardness measurement, it was possible to estimate, by extrapolation, the hardness of the very thin layer that formed at the top surface of the treated sample.

At the micrometre scale, the morphology of the nitrided layer was observed using a scanning electron microscope in back-scattered electron imaging mode (SEM – BSE mode) while the elemental composition was quantitatively measured using an electron probe micro-analyzer (EPMA). SEM observations were performed on a Philips XL30 S-FEG microscope operating in the backscattered electron imaging mode at an acceleration voltage of 25 kV. The EPMA measurements were carried out on a JEOL JXA 8530-F electron probe micro-analyser with an acceleration voltage at 15 kV and a probe current at 30 nA. Depth profiles were carried out to determine the elemental distribution of nitrogen (N), iron (Fe) and aluminium (Al) with depth. Profiles were performed directly on the cross-section of the sample, from the topmost surface of the nitrided layer to the substrate material with a step size of 1  $\mu\text{m}$ . The analyser spectrometers were calibrated with standards before measurements: an  $\text{Al}_2\text{O}_3$  standard was used to quantify the amount of Al while Fe and N were quantified using a  $\gamma'$ - $\text{Fe}_4\text{N}$  standard. The conventional ZAF matrix correction procedure was used to calculate the weight and atomic compositions from the measured X-ray intensities [33]. The crystalline phase identification of the nitrided layer was carried out on a INEL CPS 120 diffractometer using a grazing incidence X-ray diffraction (GIXRD) geometry. The GIXRD measurements were conducted at various incidence angles ( $\alpha = 6^\circ$  and  $3^\circ$ ) using a  $\text{Co-K}_\alpha$  incident radiation ( $\lambda = 0.17903 \text{ nm}$ ). GIXRD patterns were recorded in the  $2\theta = 30^\circ - 115^\circ$  angular range, with a step size of  $0.027^\circ$  and 25 s per step.

At the micro- and nanometre scale, transmission electron microscopy (TEM) and atom probe tomography (APT) were conducted. Specimens for TEM and APT were prepared within the nitrided layer using a focused ion beam (FIB) microscope (Zeiss® NVision-40). For TEM, the foil was extracted from a mirror polished cross section of

the nitrided specimen. It was prepared perpendicular to the specimen surface, at the midpoint between the surface and the bulk. Specimens for APT were lifted-out from the same cross-section, but parallel to the sample surface, at a depth of  $3 \pm 0.1 \mu\text{m}$ . These specimens were thinned to their final dimensions ( $< 70 \text{ nm}$  in thickness for the TEM foil, and to a final radius of curvature of about  $50 \text{ nm}$  for the APT tip) using  $30 \text{ keV Ga}^+$  ions [34, 35]. A final milling step with  $2 \text{ keV Ga}^+$  ions was applied to reduce the ion damage on the TEM foil. TEM observations were carried out on a JEOL ARM 200 – cold FEG UHR transmission electron microscope operating at  $200 \text{ kV}$  and equipped with a Cs corrector. In scanning mode (STEM), EDS analyses (EDS elemental maps) were obtained using a DRY SD30VG energy-dispersive X-ray spectrometer with a probe size equal to  $7 \text{ nm}$  and a dwell time equal to  $5 \text{ ms}$ . The APT analyses were conducted on a CAMECA-LEAP 4000 HR, with a base temperature of  $80 \text{ K}$ , a pulse repetition rate of  $200 \text{ kHz}$  and an average detection rate of  $0.1\%$ . Several peak overlaps in APT mass spectra were encountered, and treated as follows: the common isobar between  $^{54}\text{Cr}^{++}$  and  $^{54}\text{Fe}^{++}$  was assigned to Fe, because of very low Cr concentration, and the possible overlap between  $^{27}\text{Al}^+$  and  $^{54}\text{Fe}^{++}$  was neglected in favor of Fe, as the presence of  $^{27}\text{Al}^+$  is marginal in Fe based materials. In addition, peaks at  $14$ ,  $14.5$  and  $15 \text{ Da}$  were assigned to  $\text{N}^+$  and  $\text{N}_2^{++}$  ions. The presence of  $\text{N}_2^{++}$ , manifested by the  $(^{14}\text{N}-^{15}\text{N})^{++}$  peak at  $14.5 \text{ Da}$ , signifies that the peak at  $14 \text{ Da}$  is also composed of  $(^{14}\text{N}-^{14}\text{N})^{++}$  in addition to  $^{14}\text{N}^+$  ions. From the natural abundance of N isotopes, according to the procedure described in [36],  $38 \%$  of counts in the main peak at  $14 \text{ Da}$  are due to  $(^{14}\text{N}-^{14}\text{N})^{++}$  ions. This correction was applied for the quantitative data in table 1, but not on the illustrating concentration profiles provided in Fig. 7c. Also, the standard deviations



indicated on concentration profiles are calculated from detection statistics [37], but do not include the uncertainty due to the presence of  $N_2^{++}$  ions.

### 3. Results and discussion

The SEM micrograph in Fig. 1a reveals two distinct sublayers throughout the nitrided layer depth: a 1-2  $\mu\text{m}$ -thick outer sublayer on the topmost surface (see close-up micrograph in Fig. 1c) and a 34 - 36  $\mu\text{m}$ -thick inner sublayer directly in contact with the substrate. The first outer sublayer is thin and appears quite homogeneous within its thickness. The second inner sublayer is thick and presents two specific features which will be the subject of a close examinations in the present study: i) a network of light contrasted “wave-like” veins of 1 – 3  $\mu\text{m}$  in length that mainly follow the grain boundaries and are preferentially extended parallel to the surface (Fig. 1b) and ii) some light contrasted segregated “nodular-like” domains of 500 nm - 1  $\mu\text{m}$  in diameter located in the inner nitrided layer (marked in Fig. 1a and 1c). It is also worth noting that the BSE imaging mode used here being strongly related to the atomic number of the probed elements, suggests that the brighter areas observed in the Fig. 1a-c (the thin outer sublayer, the “wave-like” veins and the “nodular-like” regions) are much richer in Fe than in Al.

Micro-hardness results carried out on the nitrided layer are given in Fig. 2a-b. As depicted in the experimental part, two hardness measurement protocols were used: a first which consisted in performing indentations on the sample surface with increasing loads (50, 100, 300, 500 and 1000 g) (Fig. 2a) and a second which consisted in carrying out an indentation line scan-profile on the sample cross-section at constant load (100 g) (Fig. 2b). The Fig. 2a highlights differences in the hardness between the topmost

nitrided surface (about 870 Hv evaluated from the lowest indentation load of 50 g at the minimum penetration depth of 1.4  $\mu\text{m}$ ) and the remaining nitrided layer (about 1390 Hv evaluated with the highest indentation load of 1000 g at the maximum penetration depth of 5.2  $\mu\text{m}$ ). Such differences are caused by the presence of the thin outer sublayer (1-2  $\mu\text{m}$  in thickness) which exhibits lower mechanical properties and surely different microstructural characteristics compared to the inner nitrided sublayer. This point will be further explored within the next section. The micro-hardness line scan-profile given in Fig. 2b evidences the strong surface hardening of the FeAl40 Grade 3 iron aluminide when subjected to the nitriding treatment. While the hardness of the base material is about 410 Hv, the hardness of the inner nitrided layer is about 1400 Hv. It is also worth noting that a good agreement is observed between the two protocols of the micro-hardness measurement that were applied since the hardness value measured on the top surface using the maximum load ( $\text{Hv}_{1000\text{g}} = 1390$  in Fig. 2a) is very close to the one measured within the inner layer ( $\text{Hv}_{100\text{g}} = 1400$  in Fig. 2b).

EPMA-depth profiles recorded along the cross-section of the nitrided layer are given in Fig. 3. Concerning the outer sublayer, the EPMA analysis performed at 1  $\mu\text{m}$ -depth show that the nitrided layer consists mainly in Fe and N and is totally depleted in Al. The strong presence of Fe and the absence of Al in the outer sublayer are consistent with the image contrast of the previous SEM observations carried out under the BSE imaging mode (Fig. 1). Moreover, the atomic ratio N / Fe is about 0.24 which is very close to the  $\gamma'$ -Fe<sub>4</sub>N iron nitride composition. This is confirmed with the XRD patterns given in Fig. 4 which were recorded in grazing-incidence geometry on the nitrided surface. Indeed, the increase in the relative intensity of the  $\gamma'$ -Fe<sub>4</sub>N peaks with the decrease in the incidence  $\alpha$ -angle (from 6° to 3°) of the X-ray beam evidences that  $\gamma'$ -

Fe<sub>4</sub>N is preferentially located at the topmost surface of the nitrided material. The presence of the  $\gamma'$ -Fe<sub>4</sub>N iron nitride in the thin outer sublayer explains the lower value in the hardness (870 Hv) measured at the topmost surface with the minimum indentation load (50 g). Interestingly, the extrapolation of the hardness data in Fig. 2a gives a hardness range between 500 and 800 Hv for this outer sublayer which is rather consistent with the values reported in the literature for the  $\gamma'$ -Fe<sub>4</sub>N iron nitride [38, 39].

In their pioneer work on the nitriding of a Fe-40 at.% Al alloy, the presence of the  $\gamma'$ -Fe<sub>4</sub>N on the processed surface was also observed by Spies et al. [28]. Using a sufficiently high temperature to enable Fe atoms mobility (> 550 °C) and a sufficiently high nitriding potential  $K_N$  (>1) to control the nitrogen supply at the surface, they propose that the diffusion of Fe atoms towards the nitrogen located at the surface is the main mechanism for the growth of such iron nitride layer at the topmost surface. The nitriding conditions used in the present study are close to those recommended by Spies et al. [28] since the nitriding temperature was set at 600 °C and the pulsed dc-plasma nitriding process ensures a high nitrogen supply at the processed surface [30]. More recently, the unusual formation of  $\gamma'$ -Fe<sub>4</sub>N at the nitrided surface was also reported by Meka et al. [40] upon nitriding a Fe-4.75 at.% Al alloy. They proposed that the growth of the  $\gamma'$ -Fe<sub>4</sub>N iron nitride is due to the negligible solubility of Al within  $\gamma'$ -Fe<sub>4</sub>N in association with the obstructed precipitation of the AlN aluminium nitride in the  $\alpha$ -Fe ferrite. This results in the nucleation and the growth of a  $\gamma'$ -Fe<sub>4</sub>N needles which deeply penetrates the nitrided layer (up to about 40  $\mu$ m from the surface). Although this mechanism is well adapted to describe the formation of the  $\gamma'$ -Fe<sub>4</sub>N phase during nitriding of Fe-Al alloys with low Al content (4.75 at.% Al), it remains debatable for Al-rich Fe-Al alloys for which  $\gamma'$ -Fe<sub>4</sub>N is developed as a thin layer at the top most

surface (less than 2  $\mu\text{m}$ ). In addition, it is not easy to explain where the aluminium atoms which are rejected from the  $\gamma'$ -Fe<sub>4</sub>N superficial layer are going since no accumulation of Al is observed at the outer / inner sublayer interface. Finally, another possible explanation which could explain the absence of Al in the outer sublayer consists in considering the selective evaporation of this element due to a local higher temperature at the topmost surface of the processed sample compared to the bulk material (where the temperature probe is located). Indeed, it is quite possible that some “edge” effects take place at the extreme surface of the processed sample mainly due to the ionic bombardment of the surface and the local distribution of the electric field at the vicinity of the cylindrical processed sample. These “edge” effects are known to promote a slight increase of the temperature locally at the topmost surface. This last explanation should be the subject of further investigations.

Concerning the inner nitrided sublayer, the EPMA-depth profile given in Fig. 3 shows the presence of both the Fe, Al and N elements. A weak composition gradient is observed from the surface to the substrate (36 to 40 at.% Fe, 37 to 33 at.% N and 26 to 24 at.% Al). As discussed previously, and taking into account that  $\gamma'$ -Fe<sub>4</sub>N is associated to the outer sublayer, the GIXRD patterns given in Fig. 4 tend to indicate that the inner sublayer consists in both the hex. AlN aluminium nitride and the  $\alpha$ -Fe ferrite. As the atomic ratio N / Al is higher than 1, an excess in nitrogen is reported into the inner sublayer which contains more nitrogen than necessary for precipitation of all Al atoms as AlN together with the equilibrium saturation with nitrogen in the  $\alpha$ -Fe solid solution. Although the storage of this amount of excess nitrogen is still the subject of discussion, a widespread explanation in the literature considers that the nitrogen atoms in excess could be trapped at dislocations, phase interfaces and within the strained  $\alpha$ -Fe ferrite

lattice [40, 41, 44-53]. As will be discussed hereafter, it is also possible that some excess N atoms form  $N_2$  molecules that coalesce in residual porosity.

After crossing the nitrided layer / metal substrate interface, the N concentration drops sharply to zero while the Fe and Al amounts increase to reach the base composition of the FeAl40 Grade 3. Such a sharp decrease in the nitrogen content indicates that there is no diffusion zone or chemical gradient in the base substrate. Consequently, this suggests that the interaction of Al atoms in the B2 bcc-ordered matrix and the diffusing nitrogen is of a strong character, which is known to give rise to domains separated with a sharp diffusion boundary [28]. The combination of the Al and the N atoms to form the hex. AlN aluminium nitrides results in the decomposition of the ordered B2 FeAl base material structure and the appearance of the  $\alpha$ -Fe ferrite structure as indexed on the GIXRD patterns provided in Fig. 4.

At a sub-micrometre scale, the TEM micrographs given in Fig. 5a show that the “wave-like” veins of about 100 nm in width are interconnected and join the segregated “nodular-like” domains. The STEM / EDS elemental maps shown in Fig. 5b and the quantitative elemental analysis reported in Table 1 evidence that the “wave-like” veins and the “nodular-like” domains are exclusively composed of Fe atoms which crystallized into the  $\alpha$ -Fe ferrite bcc-structure consistently with the previous GIXRD phase identification (Fig. 4). Without having determined the crystallographic structure and the elemental composition of such “wave-like” veins, Spies et al. [28] were the first to report their presence within the nitrided layer of a Fe-40at.% Al iron aluminide alloy. Recently, Zhang et al. [29] have shown that these veins are rich in Fe and they proposed a mechanism for their formation. Taking into account both the diffusion of N through the original FeAl grain boundaries and the strong interaction character between Al and

N to form the aluminium nitride, they suggested that the N atoms preferentially located along the grain boundaries attract the Al atoms leaving behind the centre of the nitrified grains depleted in Al and enriched in Fe. Assuming this explanation, the Fe-rich “wave-like” veins should be located intragranularly and not at the grain boundaries. This is clearly not the case since SEM observations such as the micrographs given in Fig. 1b clearly evidence that: i) these  $\alpha$ -Fe “wave-like” veins are mainly located at the grain boundaries and ii) they are preferentially aligned parallel to the nitrified surface. Looking at the literature corresponding to other systems, the presence of similar intergranular veins was also observed in nitrified chromium-alloyed steels. Van Wiggeren et al. [41] were the first to report the presence of  $\text{Fe}_3\text{C}$  cementite at the grain boundaries of the steel matrix. With prolonged nitriding time, they showed that the percolation of these cementite domains results in veins preferentially aligned with respect to the nitrified surface. Shortly after, using quite the same type of alloyed steel and applying quite the same nitriding conditions, Barrallier et al. [42] and Traskine et al. [43] proposed a mechanism of formation of these oriented carbides. They established that the probability of the  $\text{Fe}_3\text{C}$  cementite precipitation is strongly dependent on the orientation of the grain boundary with respect to the local stress axis generated in the nitrified layer during the nitriding process. Specifically, they showed that the nucleation of the  $\text{Fe}_3\text{C}$  precipitates is promoted for the grain boundaries which are oriented parallel to the nitrified surface because they correspond to the macroscopic plane of the maximum compressive stress. The TEM micrographs in Fig. 5a and the STEM / EDS elemental maps in Fig. 5b show the presence of porosities of about 200 nm in diameter (appearing in dark under the dark field imaging in Fig. 5b) which are precisely located within the Fe-rich “nodular-like” region. In the case of nitriding of iron-based metallic alloys, and

to the best of our knowledges, few authors have reported and discussed the formation of pores in nitrided layers [41, 44, 45]. They proposed that the formation of pores proceeds by the local recombination of N atoms initially dissolved in the  $\alpha$ -Fe ferrite phase, to form  $N_2$  molecules which coalesce and produce voids containing nitrogen gas. The fact that these pores are located within the Fe-rich “nodular-like” regions, often at the intersection of several  $\alpha$ -Fe veins (Fig. 5a-b), suggest that this mechanism can also be valid for the nitriding of the investigated FeAl40 Grade3 alloy.

At the tens of nanometre scale, the TEM micrograph in Fig. 6a shows the presence of a “lamellar-like” morphology which fills the space between the  $\alpha$ -Fe “wave-like” veins. The TEM micrographs also reveal the occurrence of many differently oriented colonies of lamellae which start from the original FeAl grain boundaries. The lamellae exhibit a length of about 300 nm on average (Fig. 6a) and a width of 10 nm (Fig 6c). The STEM /EDS elemental maps given in Fig. 6b show that Fe-rich lamellae alternate periodically with Fe-lean lamellae, the latter being mainly composed of Al and N and in lower amount of Fe. This results was confirmed with the APT elemental quantification performed locally on each type of lamella and reported in Table 1. The selected area electron diffraction (SAED) pattern recorded on a colony of lamellae (Fig. 6a) reveals the presence of both the hex. AlN aluminium nitride and the  $\alpha$ -Fe ferrite while the Fourier fast transform (FFT) pattern performed locally on a single Fe-rich lamella shows the exclusive presence of the  $\alpha$ -Fe ferrite (Fig. 6c). Consequently, it could be deduced that the observed lamellar morphology consists in  $\alpha$ -Fe lamellae which alternate periodically with AlN /  $\alpha$ -Fe lamellae. The growth of such a “lamellar-like” morphology has been widely reported in the literature dealing with the nitriding of iron-based alloys, for example in the binary Fe-Cr and Fe-V alloys and the

ternary Fe-Cr-C alloys [46-48, 53]. The similarity between the lamellar morphology observed in the nitrided Fe-1wt.% Cr alloys forming CrN /  $\alpha$ -Fe lamellae or in the nitrided Fe-2 wt.% V alloys forming VN /  $\alpha$ -Fe lamellae and the lamellar morphology observed in the present nitrided material strongly suggests that the nitriding of the FeAl40 Grade 3 alloy proceeds also through a mechanism of discontinuous precipitation. With the exception of Zhang et al. [29], who were recently the first to observe this lamellar morphology in the FeAl40 Grade 3 alloy but without mentioning the possibility of a discontinuous precipitation mechanism, the growth of this specific lamellar morphology has never been reported in the literature for the nitriding of the Fe-Al binary alloys [49-52]. This could be explained by the fact that most of the referenced studies remains focused on the nitriding of Fe-Al alloys with low amount of Al (a maximum of 4.75 at.% Al for Ref. [52]) for which the precipitation proceeds only according to a “continuous” mechanism. In comparison, in the case of iron-based alloys (Fe-Cr, Fe-V and Fe-Cr-C alloys), it has been established that the concentration in the alloying elements is the main factor that influences the amount of discontinuously transformed areas in the nitrided layer [47, 48, 53]. The larger the concentration in Cr or V alloying elements in the alloy, the larger the amount of discontinuous precipitation taking place in the ferritic matrix. For example, it has been demonstrated that below 1wt.% of Cr, the nitrided Fe-Cr alloy shows only a “continuous” precipitation morphology with dispersed coherent submicroscopic CrN “platelet-like” nitrides. Comparatively, in the range of 1-13 wt.% of Cr, the “continuous” precipitation mechanism is concomitant with a “discontinuous” precipitation of CrN /  $\alpha$ -Fe lamellae, the latter occurring only in few grains of the nitrided layer. Finally, with amounts in Cr above 13 wt.%, the nitriding process involves only a “discontinuous” precipitation for



which the resulting CrN /  $\alpha$ -Fe lamellar morphology covers the whole nitrided layer. In our case, these literature results suggest that the “discontinuous” precipitation is the main mechanism involved for the nitriding of the FeAl40 Grade 3 because of its high amount of Al.

At the nanometre and atomic scales, the APT analyses presented in Fig. 7a-b and reported in Table 1 were carried out in a probed volume spreading over a Fe-rich lamella and a Fe-lean lamella. Within the Fe-lean lamella, a finer structural arrangement is observed in which Fe-lean clusters are separated by Fe-rich walls. The detailed spatial distribution of Al, Fe and N species through a 3 nm thick cross-section described by the rectangle in solid lines in Fig. 7a supports the same description. This is shown in Fig. 7b where a Fe-rich region located on the left hand side corresponds actually to the  $\alpha$ -Fe lamellae. On the right hand side, within the hex. AlN /  $\alpha$ -Fe lamellae, the Al and N species are localized in Fe-lean clusters (~6 nm in thickness) which are trapped between two successive thin Fe-rich walls (~2 nm in thickness) (Fig. 7c). Combined with the high resolution TEM results given in Fig. 6, it is reasonable to expect that these Fe-rich walls are composed of  $\alpha$ -Fe phase while the Fe-lean clusters probably consists in a hex. AlN /  $\alpha$ -Fe mixture structured at the nanometric scale.

#### **4. Conclusion**

A binary B2 bcc-ordered FeAl40 Grade 3 iron aluminide was nitrided at 600 °C for 15 min with a pulsed DC plasma in a 95% N<sub>2</sub> / 5% H<sub>2</sub> gas mixture. The microstructure of the nitrided layer was fully described at the micro-, nano- and atomic scales in order to propose a better understanding of the nitriding mechanisms that occurs in Al-rich Fe-Al alloy (40 at.% Al)

Within the nitriding conditions used, the nitrided layer consisted of two sublayers have very different characteristics :

- An outer sublayer form at the top surface because of a sufficiently high nitriding temperature (600 °C) combined with the use of the pulsed-dc plasma nitriding technology which ensures a high nitrogen supply at the metal surface. This resulted in the formation of a thin outer sublayer composed of the  $\gamma'$ -Fe<sub>4</sub>N iron nitride (~1-2  $\mu\text{m}$  in thickness) which exhibits a moderate hardness (between 550 and 850 Hv).
- An inner sublayer which is thicker (36  $\mu\text{m}$  in thickness) and harder (1400 Hv). Within this inner sublayer, the strong interaction character between the Al atoms with the diffusing N atoms results in the formation of the hex. AlN aluminium nitride and the decomposition of the B2 bcc-ordered structure (fully depleted in Al) into the  $\alpha$ -Fe ferritic structure. An excess in nitrogen was revealed in this sublayer. In addition to possible N trapping at dislocations, interfaces or within the strained lattice the presence of porosity was revealed which was attributed to recombination of N atoms, initially present in the  $\alpha$ -Fe ferrite phase, to form N<sub>2</sub> gas molecules and porosity exclusively located at the intersection of  $\alpha$ -Fe veins.

The microstructure within the inner sublayer was rather complex and revealed a number of interesting additional features at different scales of analysis:

- The  $\alpha$ -Fe phase formed during the nitriding process followed an intergranular network of  $\alpha$ -Fe “wave-like” veins (1-3  $\mu\text{m}$  in length, ~100 nm in width) that were essentially oriented along the grain boundaries parallel to the nitrided

surface. It is suggested that they form specifically at these boundaries because they experience the maximum compressive stress.

- When submitted to nitriding, the FeAl40 Grade 3 containing high amount of Al (40 at.% Al) is subjected to a mechanism of “discontinuous” precipitation. This mechanism leads to the growth of a “lamellar-like” microstructure which starts from the grain boundaries and fills the space between the  $\alpha$ -Fe “wave-like” veins. The lamellar morphology is composed of  $\alpha$ -Fe lamellae which alternate periodically with AlN/ $\alpha$ -Fe lamellae (300 nm in length, 10 nm in thickness).
- The formation of lamellae containing both  $\alpha$ -Fe and AlN is rather unusual. The observations conducted by high resolution transmission electron microscopy and atom probe tomography show that within an AlN /  $\alpha$ -Fe lamella, a finer structural arrangement is observed with the presence of AlN rich clusters (~6 nm in thickness) separated by thin  $\alpha$ -Fe walls (~2 nm thick).

The diversity of the morphologies evidenced in the present study highlights the complexity of the nitriding mechanisms of iron-based aluminides, particularly those containing large amounts of Al. Further experiments and analysis should be undertaken to confirm the proposed mechanisms of formation of the multi-scale morphological features observed in the present study.

## **Acknowledgments**

This work and the post-doctoral stay of A. Martinavicius were supported by the French Government through the program "Investissements d'avenir" operated by the French National Research Agency (ANR) and referenced to as ANR-11-LABX-0008-01

(LabEx DAMAS). The authors would like to thank Dr.-Ing. P. Boulet (Institut Jean Lamour, CC X-Gamma) for grazing incidence XRD measurements.

## References

- [1] I. Baker, A review of the mechanical properties of B2 compounds, *Mater. Sci. Eng. A* 192-193 (1995) 1-13.
- [2] C.T. Liu, E.H. Lee, C.G. McKamey, An environmental effect as the major cause for room-temperature embrittlement in FeAl, *Scripta Metall.* 23 (1989) 875-880.
- [3] F. Moret, R. Baccino, P. Martel, L. Guetaz, Properties and applications of B2-FeAl intermetallic alloys, *J. Phys. IV* 6 (1996) 281-289.
- [4] M.A. Munoz-Morris, C. Garcia Oca, D.G. Morris, An analysis of strengthening mechanisms in a mechanically alloyed, oxide dispersion strengthened iron aluminide intermetallic, *Acta Mater.* 50 (2002) 2825-2836.
- [5] M.A. Montealegre, J.L. Gonzalez-Carrasco, Influence of the yttria content on the oxidation behaviour of the intermetallic Fe40Al alloy, *Intermetallics*, 11 (2003) 169-175
- [6] M. Berlanga, J.L. Gonzalez-Carrasco, M.A. Montealegre, M.A. Munoz-Morris, Oxidation behaviour of yttria dispersion strengthened Fe40Al alloy foils, *Intermetallics*, 12 (2004) 205-212
- [7] M.A. Munoz-Morris, C. Garcia Oca, D.G. Morris, Microstructure and room temperature strength of Fe-40Al containing nanocrystalline oxide particles, *Acta Materialia* 51 (2003) 5187-5197.
- [8] G. Ji, T. Grosdidier, F. Bernard, S. Paris, E. Gaffet, S. Launois, Bulk FeAl nanostructured materials obtained by spray forming and spark plasma sintering, *J. Alloys and Compounds* 434 (2007) 358-361.
- [9] T. Skiba, P. Hauslid, M. Karlik, K. Vanmeensel, J. Vleugels, Mechanical properties of spark plasma sintered Fe-Al intermetallics, *Intermetallics*, 18 (2010) 1410-1414

- [10] T. Grosdidier, G. Ji, N. Bozzolo, Hardness, thermal stability and yttrium distribution in nanostructured deposits obtained by thermal spraying from milled - Y2O3 reinforced - or atomized FeAl powders, *Intermetallics*, 14 (2006) 715-721
- [11] R. Musalek, O. Kovarik, T. Skiba, P. Hauslid, M. Karlik, J. Colmenares-Angulo, , Fatigue properties of Fe-Al intermetallic coatings prepared by plasma spraying, *Intermetallics*, 18 (2010) 1415-1418
- [12] G. Rolink, S. Vogt, L. Sencekova, A. Weisheit, R. Poprawe, M. Palm, J. , Laser metal deposition and selective laser melting of Fe-28 at% Al, *Materials Research*, 29 (2014) 2036-2043.
- [13] Industrial Applications of FeAl40Grade3, a high specific properties Iron Aluminides DOI: 10.1002/3527607285.ch52
- [14] T. Grosdidier, G. Ji, S. Launois, Processing dense hetero-nanostructured metallic materials by spark plasma sintering, *Scripta Materialia* 57 (2007) 525-528.
- [15] T. Grosdidier, E. Suzon, F. Wagner, Primary recrystallization in an ODS FeAl alloy: an effective way to modify texture and microstructure, *Intermetallics* 12 (2004) 645-654.
- [16] S. Guessasma, E. Suzon, T. Grosdidier, Static recrystallisation in an ODS FeAl alloy: The effect of particles on texture and anisotropic grain growth developments, F. Wagner, *Intermetallics* 16 (2008) 1013-1025.
- [17] D.G. Morris, M.A. Munoz-Morris, *Materials Science and Engineering A* 596 (2014) 165-169.
- [18] N.S. Stoloff, C.T. Liu, Review: Environmental embrittlement of iron aluminides, *Intermetallics* 2 (1994) 75-87

- [19] C.T. Liu, E.P. George, P.J. Maziasz, J.H. Schneibel, Recent advances in B2 iron aluminide alloys : deformation, fracture and alloy design, *Materials Science and Engineering A*, 258 (1998) 84-98.
- [20] D. Risanti, J. Deges, L. Falat, S. Kobayashi, J. Konrad, M. Palm, B. Pöter, A. Schneider, C. Stallybrass, F. Stein, Dependence of the brittle-to-ductile transition temperature (BDTT) on the Al content of Fe-Al alloys, *Intermetallics*, 13 (2005) 1337-1342.
- [21] G. Ji, F. Bernard, S. Launois, T. Grosdidier, Processing conditions, microstructure and mechanical properties of hetero-nanostructured ODS FeAl alloys produced by spark plasma sintering, *Materials Science and Engineering A* 559 (2013) 566-573
- [22] H.E. Maupin, R.D. Wilson, J.A. Hawl, Deformation of ordered Fe-Al intermetallic alloys, *Wear* 162-164 (1993) 432-440
- [23] J. Qiu, I. Baker, F.E. Kennedy, Y. Liu, P.R. Munroe, The effects of stoichiometry on the dry sliding wear of FeAl, *Intermetallics* 40 (2013) 19-27
- [24] J. Xia, C.X. Li, H. Dong, Thermal oxidation treatment of B2 iron aluminide for improved wear resistance, *Wear* 258 (2005) 1804-1812
- [25] K. Nowak, M. Gupta, The effect of pre-oxidation treatment on the plasticity behavior of B2 iron aluminide, *Vacuum*, 90 (2013) 10-16.
- [26] E. Ekmekçiler, A. Polat, M. Usta, Hard boride coating on iron aluminide (FeAl), *Surf. Coat. Technol.* 202 (2008) 6011-6015
- [27] F. Pedraza, J.L. Grosseau-Poussard, J.F. Dinhut, Nitridation effects on the oxidation mechanisms of an ods Fe-Al intermetallic alloy, *Appl. Surf. Sci.* 233 (2004) 35-41.

- [28] H.J. Spies, H. Biermann, A. Fischer, Nitriding behaviour of the intermetallic alloy FeAl, *Z. Metallkd.* 96 (2005) 781-786.
- [29] Z. Zhang, X. Li, H. Dong, Plasma-nitriding and characterization of FeAl<sub>40</sub> iron aluminide, *Acta Mater.* 86 (2015) 341-351.
- [30] T. Czerwec, H. Michel, E. Bergmann, Low pressure, high density plasma nitriding : mechanisms, technology and results, *Surf. Coat. Technol.* 108 (1998) 182-190.
- [31] S.K. Kang, J.Y. Kim, C.P. Park, H.U. Kim, D. Kwon, Conventional Vickers and true instrumented indentation hardness determined by instrumented indentation tests, *J. Mater. Research* 25 (2010) 337-343.
- [32] Y. Samih, G. Marcos, N. Stein, N. Allain, E. Fleury, C. Dong, T. Grosdidier, Microstructure modifications and associated hardness and corrosion improvements in the AISI 420 martensitic stainless steel treated by high current pulsed electron beam (HCPEB), *Surf. Coat. Technol.* 259 (2014) 737-745.
- [33] J.L. Pouchou, F. Pichoir, Surface film X-ray microanalysis, *Scanning* 12 (1990) 212-224.
- [34] L. Giannuzzi, F. Stevie, Introduction to Focused Ion Beams, Instrumentation, Theory, Techniques and Practice, Springer, USA, 2005.
- [35] D.J. Larson, T.J. Prosa, R.M. Ulfig, B.P. Geiser, T.F. Kelly, Local Electrode Atom Probe Tomography. New York, NY: Springer New York, 2013.
- [36] M. Bachhav, F. Danoix, B. Hannoyer, J.M. Bassat, R. Danoix, Investigation of O-18 enriched hematite ( $\alpha$ -Fe<sub>2</sub>O<sub>3</sub>) by laser assisted atom probe tomography, *Int. J. Mass. Spectrom.* 335 (2013) 57-60.



- [37] F. Danoix, G. Grancher, A. Bostel, D. Blavette, Standard deviations of composition measurements in atom probe analyses—Part II: 3D atom probe, *Ultramicroscopy* 107 (2007) 739–743.
- [38] N. Granito, T. Aizawa, H. Kuwahara, Wear behavior on the nitride steels, *Proceedings of the 20th ASM Heat Treating Conference Proceedings* 1-2 (2000) 347-352.
- [39] J.C. Díaz-Guillén, G. Vargas-Gutiérrez, E.E. Granda-Gutiérrez, J.S. Zamarripa-Piña, S.I. Pérez-Aguilar, J. Candelas-Ramírez, L. Álvarez-Contreras, Surface properties of Fe<sub>4</sub>N compounds layer on AISI 4340 steel modified by pulsed plasma nitriding, *J. Mater. Sci. Technol.* 29 (2013) 287-290.
- [40] S.R. Meka, E. Bischoff, R.E. Schacherl, E.J. Mittemeijer, Unusual nucleation and growth of  $\gamma'$  iron nitride upon nitriding Fe-4.75 at.% Al alloy, *Phil. Mag.* 92 (2012) 1083-1105.
- [41] P.C. Van Wigger, H.C.F. Rozendaal, E.J. Mittemeijer, The nitriding behaviour of iron-chromium-carbon alloys, *J. Mater. Sci.* 20 (1985) 4561-4582

#### Pore formation

- [42] L. Barrallier, V. Traskine, S. Botchenkov, Morphology of intergranular cementite arrays in nitride chromium-alloyed steels, *Mater. Sci. Eng. A* 393 (2005) 247-253.
- [43] V. Traskine, S. Botchenkov, Z. Skvortsova, L. Barrallier, Physicochemical mechanics of structural transformations in nitride steel, *Colloid Journal* 67 (2005) 97-102.
- [44] M.A.J. Somers, E.J. Mittemeijer, Formation and Growth of Compound Layer on Nitrocarburizing Iron: Kinetics and Microstructural Evolution  
*Surf. Eng.* 3 (1987) 123-137

- [45] B. Schwarz, H. Göhring, S.R. Meka, R.E. Schacherl, E.J. Mittemeijer, Pore formation upon nitriding iron and iron-based alloys: the role of alloying elements and grain boundaries, *Metallur. Mater. Trans. A* 45 (2014) 6173-6186.
- [46] R.E. Schacherl, P.C.J. Graat, E.J. Mittemeijer, Gaseous nitriding of iron-chromium alloys *Z. Metall* 93 (2002) 468-477
- [47] R.E. Schacherl, P.C.J. Graat, E.J. Mittemeijer, The nitriding kinetics of iron-chromium alloys; the role of excess nitrogen: Experiments and modelling, *Metall. Mater. Trans. A* 35 (2004) 3387-3398
- [48] S.S. Hosmani, R.E. Schacherl, E.J. Mittemeijer, Nitriding behavior of Fe-4wt%V and Fe-2wt%V alloys *Acta Mater.* 53 (2005) 2069-2079.
- [49] M.H. Biglari, C.M. Brakman, E.J. Mittemeijer, S. Van Der Zwaag, Analysis of the nitrogen absorption isotherms of cold-rolled Fe-2 at. % Al specimens with different AlN precipitate dimensions, *Phil. Mag. A* 72 (1995) 931-947.
- [50] M.H. Biglari, C.M. Brakman, E.J. Mittemeijer, Crystal structure and morphology of AlN precipitating on nitriding of an Fe-2at.% Al alloy *Phil. Mag* 72A (1995) 1281
- [51] S. Meka, S.S. Hosmani, A.R. Clauss, E.J. Mittemeijer The emergence and disappearance of a high density of microcracks in nitrided Fe-4.65 at.% Al alloy. *Int. J. Mater. Res.* 99 (2008) 808-814
- [52] S.R. Meka, E. Bischoff, S.S. Hosmani, E. J. Mittemeijer, Interrelationships of defects, nitride modification and excess nitrogen in nitrided Fe-4.75 at.% Al alloy. *Int. J. Mater. Research* 105 (2014) 1057-1066.
- [53] S.S. Hosmani, R.E. Schacherl, L.L. Dobrzynska, E.J. Mittemeijer, The nitrogen-absorption isotherm for Fe-21.5 at.% Cr alloy: dependence of excess nitrogen uptake on precipitation morphology *Phil. Mag.* 88 (2008) 2411-2426

## Figure captions

**Fig. 1.** (a) SEM cross-section micrograph of the FeAl40 grade 3 sample nitrided at 600 °C in 95% N<sub>2</sub> + 5% H<sub>2</sub> d.c. plasma for 15 min. showing a network of "wave-like" veins in the thick inner sublayer and the yellow circle indicates the presence of "nodular-like" segregated regions. (b) SEM cross-section micrograph evidencing the spatial distribution of the "wave-like" veins through the inner nitrided sublayer. (c) SEM cross-section micrograph highlighting the presence of "nodular-like" segregated domains through the inner nitrided sublayer.

**Fig. 2.** Variation of the hardness with depth measured: on the top surface of the nitrided sample from 1 to 5 µm depth with increasing loads (50, 100, 300, 500 and 1000 g) and on the cross-section of the nitrided sample from 5 to 76 µm depth with a constant load of 100 g.

**Fig. 3.** Chemical composition (in at%. of Fe, Al and N) of the nitrided layer determined from an EPMA line scan.

**Fig. 4.** Phase composition of the nitrided layer determined from grazing-incidence XRD measurements at various incidence angles  $\alpha = 6^\circ$  and  $3^\circ$ .

**Fig. 5.** (a) TEM micrographs of the FeAl40 grade 3 sample nitrided at 600 °C in 95% N<sub>2</sub> + 5% H<sub>2</sub> d.c. plasma for 15 min showing a network of segregated "wave-like" veins and the presence of a segregated "nodular-like" region. (b) STEM / EDS elemental maps showing the spatial distribution of Fe, Al and N over the segregated "wave-like" veins and "nodular-like" region.

**Fig. 6.** (a) TEM micrographs of the FeAl40 grade 3 sample nitrided at 600 °C in 95% N<sub>2</sub> + 5% H<sub>2</sub> d.c. plasma for 15 min showing "lamellar-like" domains and the associated

SAED pattern evidencing the presence of both  $\alpha$ -Fe and hex. AlN. (b) STEM / EDS elemental maps showing the spatial distribution of Fe, Al and N over a “lamellar-like” domain. (c) High-resolution TEM micrographs of a “lamellar-like” domain and the associated FFT pattern showing a periodic alternation of  $\alpha$ -Fe lamellae and  $\alpha$ -Fe/hex. AlN lamellae.

**Fig. 7.** (a) Reconstructed APT microstructure of the FeAl40 grade 3 nitrided at 600 °C in 95% N<sub>2</sub> + 5% H<sub>2</sub> d.c. plasma for 15 min. (b) Top-views of a 3 nm thick transverse section (indicated with a black rectangle in (a)) showing Al, Fe and N distribution. The black points referred as A, B and C line perimeter indicates regions for which the chemical composition is given in Table 1. (c) Composition profile of Al, Fe and N integrated through the cylindrical volume indicated in the Fe atoms 3D distribution (14 nm in length and 5 nm in diameter).

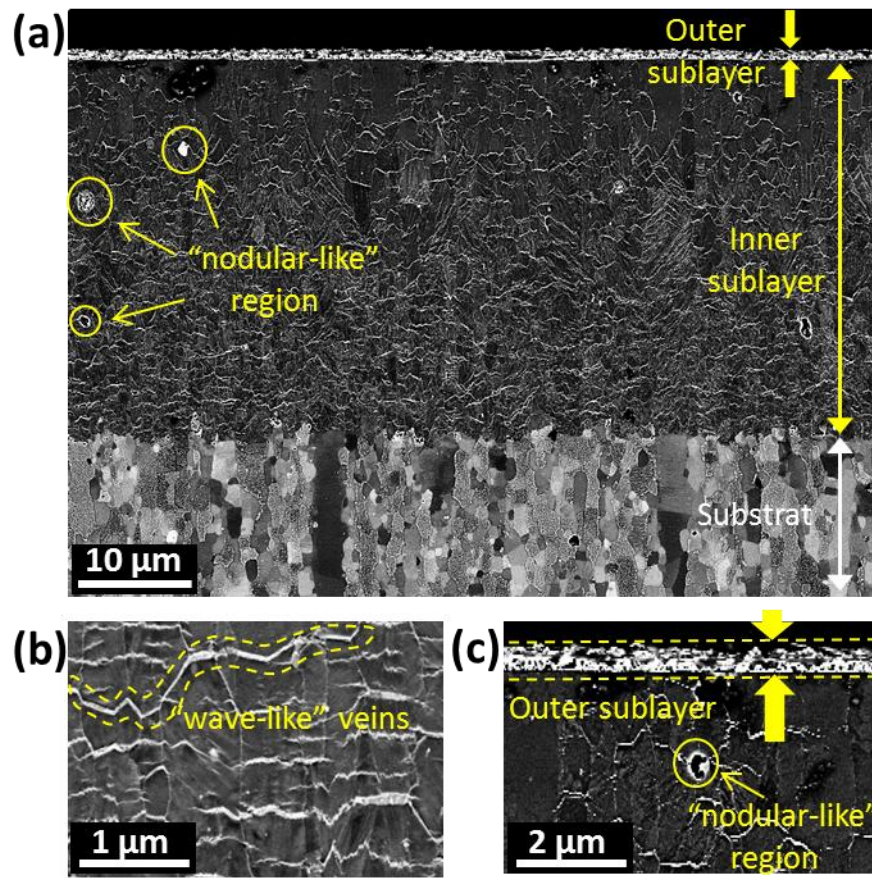
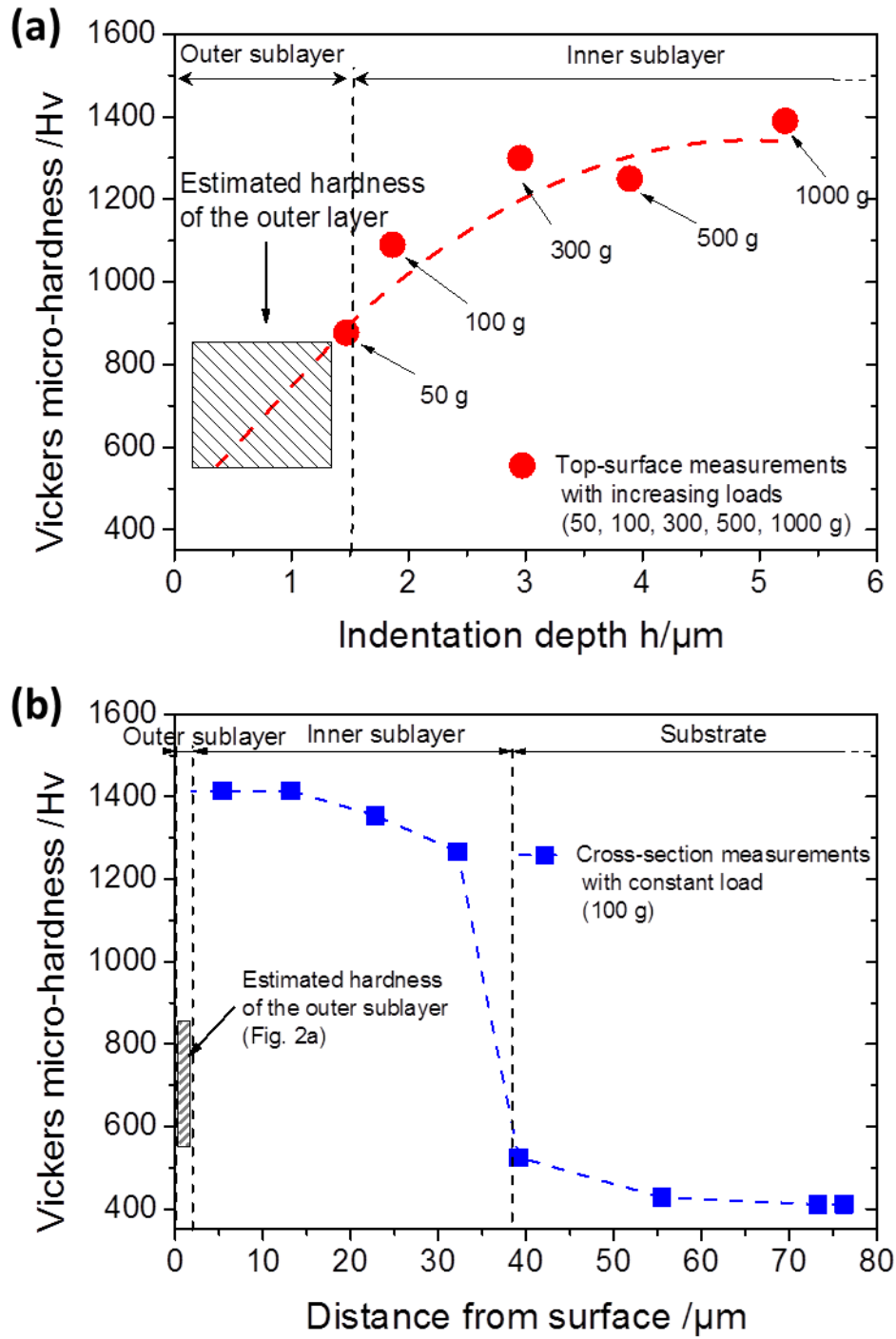


Figure 1



**Figure 2**

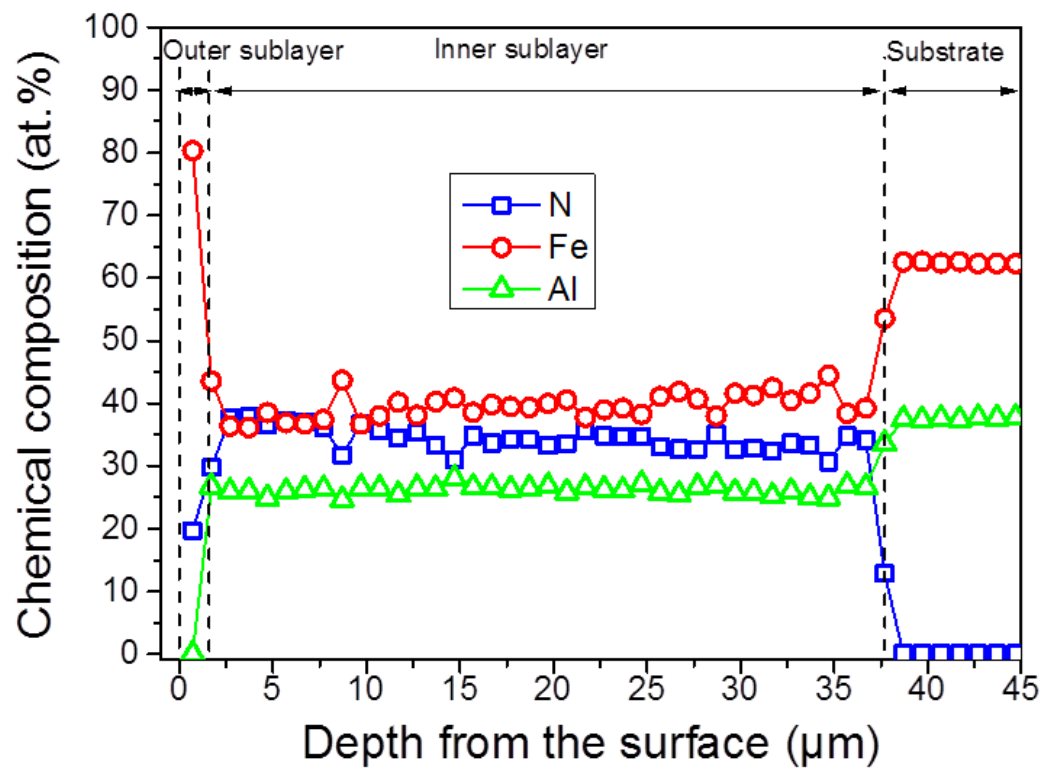
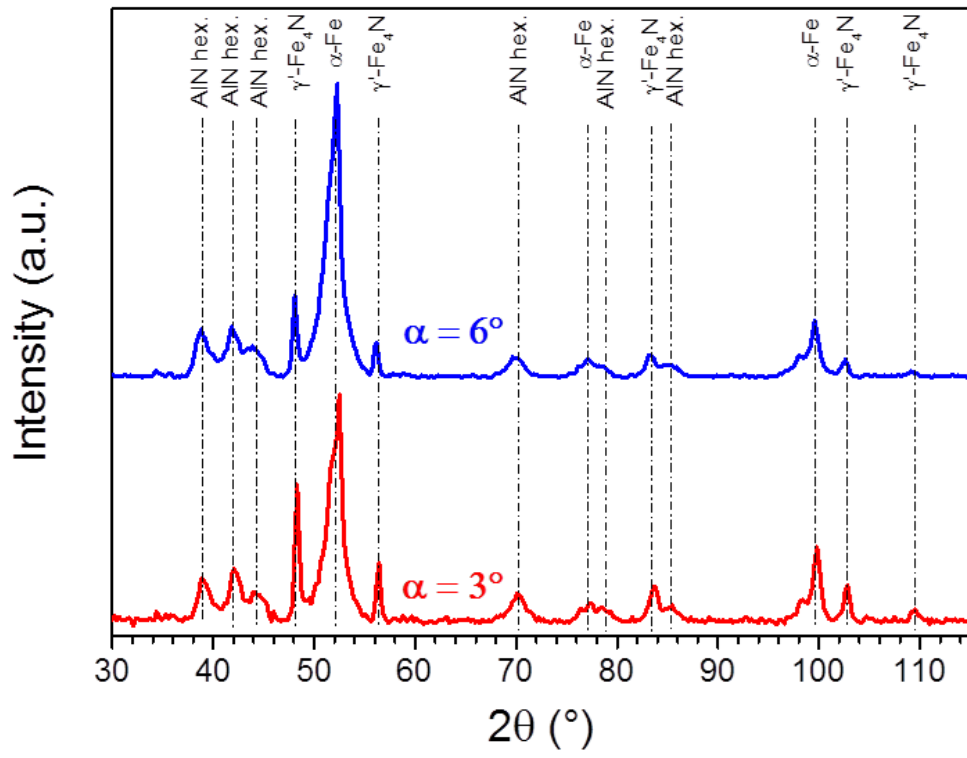


Figure 3



**Figure 4**



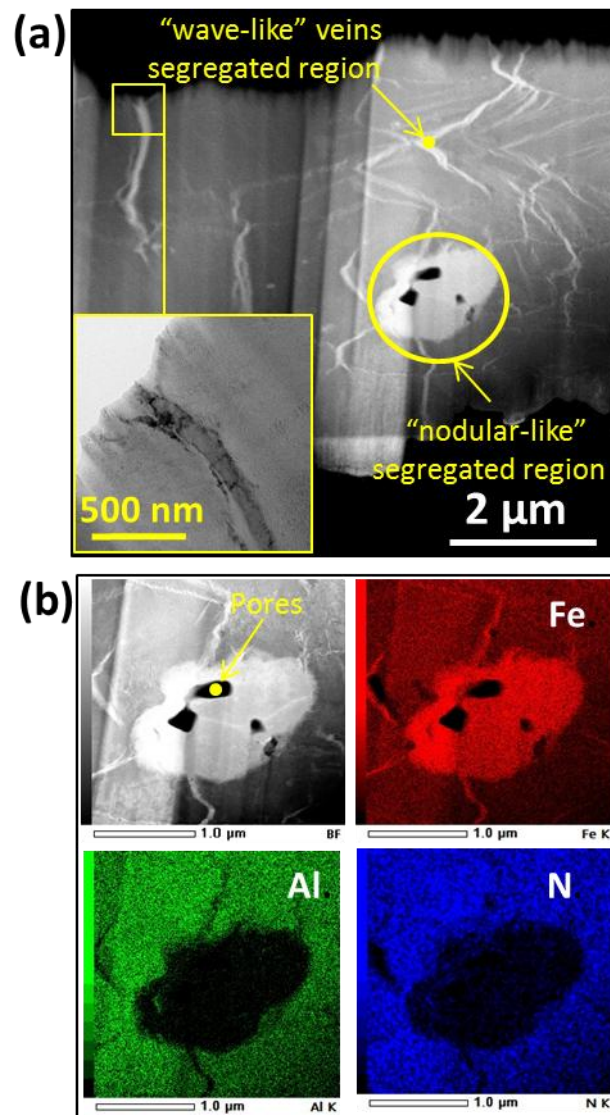


Figure 5

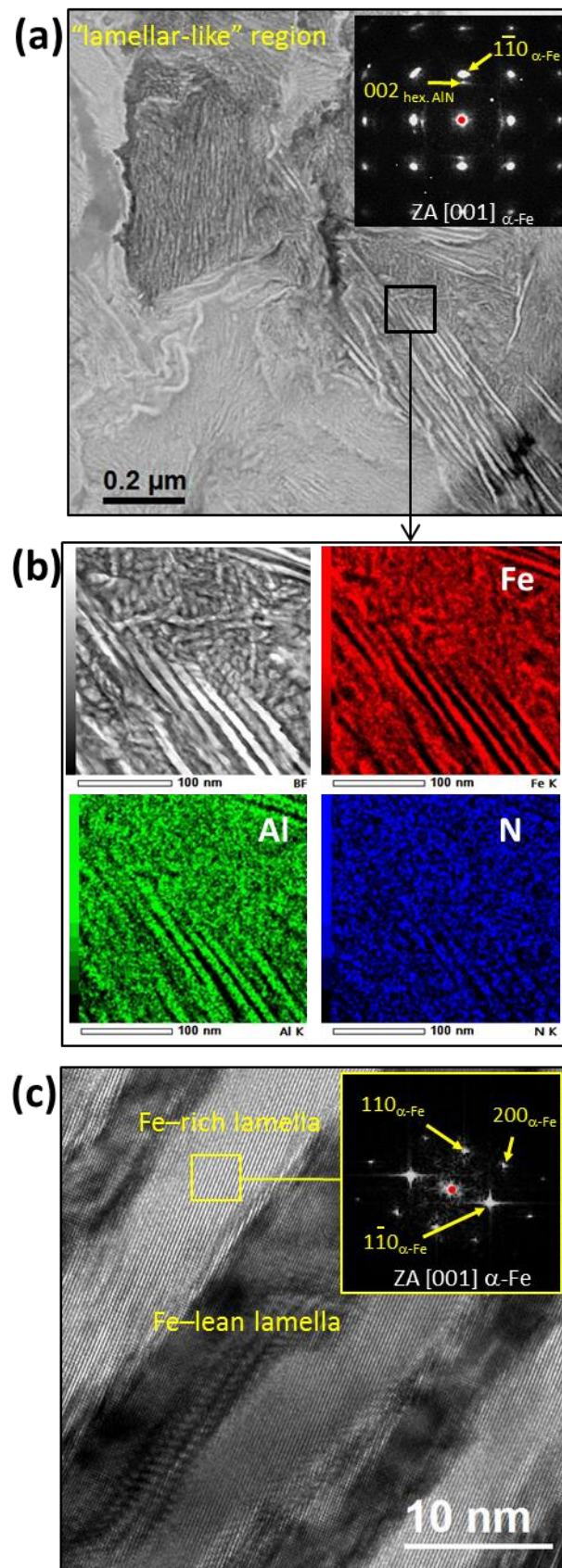
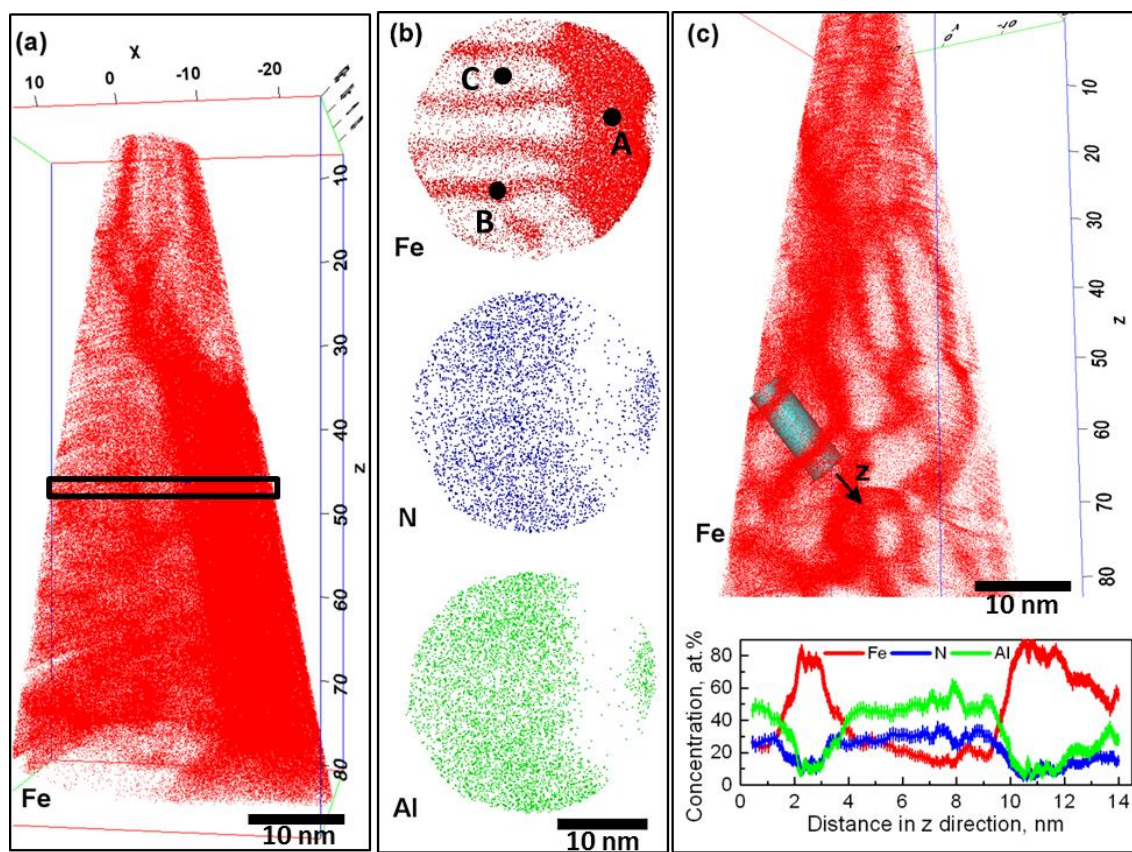


Figure 6



**Figure 7**

## Table

**Table 1.** Atomic composition of the different morphologies observed at various scales in the FeAl40 grade 3 nitrided sample at 600 °C for 15 min in a 95% N<sub>2</sub> + 5% H<sub>2</sub> d.c. plasma.

	"Wave-like"	"Nodular-like"	$\alpha$ -Fe	hex. AlN / $\alpha$ -Fe	
	region <sup>1</sup>	region <sup>1</sup>	lamellae <sup>2</sup>	lamellae <sup>2</sup>	
				Fe-rich walls	Fe-lean clusters
<b>Fe</b>	98 ± 1	100 ± 1	99.69 ± 0.02	79.82 ± 0.56	19.00 ± 0.28
<b>Al</b>	1 ± 1	-	0.03 ± 0.01	11.75 ± 0.16	48.28 ± 0.36
<b>N</b>	1 ± 1	-	0.28 ± 0.02	8.37 ± 0.14	32.31 ± 0.34
<b>Cr</b>	-	-	-	0.12 ± 0.04	0.23 ± 0.03
<b>C</b>	-	-	-	0.02 ± 0.02	0.18 ± 0.03

<sup>1</sup>From STEM/EDS analysis in regions respectively reported in **Fig. 5b**.

<sup>2</sup>From APT analysis in regions respectively marked **A**, **B** and **C** in **Fig. 7b**.